

# Highly Stretchable, Fast Self-Healing, and Waterproof Fluorinated Copolymer Ionogels with Selectively Enriched Ionic Liquids for Human-Motion Detection

Peiru Shi, Yufeng Wang, Weng Wee Tjiu, Chao Zhang,\* and Tianxi Liu

Cite This: *ACS Appl. Mater. Interfaces* 2021, 13, 49358–49368

Read Online

ACCESS |



Metrics &amp; More



Article Recommendations

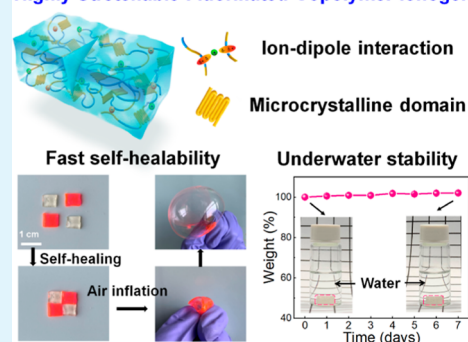


Supporting Information

**ABSTRACT:** The development of waterproof ionogels with high stretchability and fast self-healing performance is essential for stretchable ionic conductors in sophisticated skin-inspired wearable sensors but can be rarely met in one material. Herein, a semicrystalline fluorinated copolymer ionogel (SFCI) with extremely high stretchability, underwater stability, and fast self-healability was fabricated, among which hydrophobic ionic liquids ([BMIM][TFSI]) were selectively enriched in fluoroacrylate segment domains of the fluorinated copolymer matrix through unique ion–dipole interactions. Benefiting from the reversible ion–dipole interactions between the [BMIM][TFSI] and fluoroacrylate segment domains as well as the physical cross-linking effects of semicrystalline oligoethylene glycol domains, the SFCI exhibited ultrastretchability (>6000%), fast room-temperature self-healability (>96% healing efficiency after cutting and self-healing for 30 min), and outstanding elasticity. In addition, the representative SFCI also exhibited high-temperature tolerance up to 300 °C, antifreezing performance as low as −35 °C, and high transparency (>93% visible-light transmittance). As a result, the as-obtained SFCI can readily be used as a highly stretchable ionic conductor in skin-inspired wearable sensors with waterproof performance for real-time detecting physiological human activities. These attractive features illustrate that the developed ultrastretchable and rapidly self-healable ionogels with unique waterproofness are promising candidates especially for sophisticated wearable strain sensing applications in complex and extreme environments.

**KEYWORDS:** ionogels, stretchable ionic conductor, self-healing performance, wearable strain sensors, waterproof performance

## Highly Stretchable Fluorinated Copolymer Ionogels



## 1. INTRODUCTION

Skin-inspired wearable sensors that imitate human skin perception characteristics have drawn intensive attention due to their application prospects in the emerging fields of health monitoring,<sup>1–3</sup> soft robotics,<sup>4–6</sup> and human–machine interfaces.<sup>7,8</sup> Skin-inspired wearable sensors can be generally categorized into two types of electronic skins (e-skins)<sup>9,10</sup> and ionic skins (i-skins).<sup>11–13</sup> Unlike the e-skins using electric conductors that transduce response signals by electronic conduction, i-skins, using ionic conductors that sense external stimuli based on ionic conduction, are promising to achieve the functions of human skin due to the advantages of transparency, intrinsic stretchability, and high sensitivity.<sup>14–16</sup> However, i-skins are practically faced with complex deformation or continuous mechanical loading, requiring ionic conductors with high stretchability and mechanical robustness.<sup>17,18</sup> Moreover, high stability under high moistures and water environments is another important property for the durability of i-skins. Thus, the development of ionic conductors with extensive stretchability, high mechanical elasticity, and unique underwater stability is significant for the development of next-generation skin-inspired sensors.

Ionic-liquid (IL)-based gels (ionogels) that are made of ILs confined in three-dimensional polymer networks have received substantial attention owing to their unique properties of tailored ionic conductivity, wide operating temperature range, and high thermal/chemical stabilities.<sup>16,19</sup> They also have additional merits of mechanical compliance and stretchability through rational structural design, which have shown great potentials in flexible sensors,<sup>20–23</sup> energy conversions,<sup>24,25</sup> storage devices,<sup>26,27</sup> actuators,<sup>28</sup> and so forth. However, conventional ionogels are sensitive to humidity because the polymer matrix and ILs are often hygroscopic, leading to their easy swelling and degradation. A fluorinated polymer is a highly desired polymer matrix for fabricating ionogels because of its low surface energy, high humidity insensitivity, and excellent thermal/chemical stability originating from the highly

Received: August 23, 2021

Accepted: September 29, 2021

Published: October 11, 2021



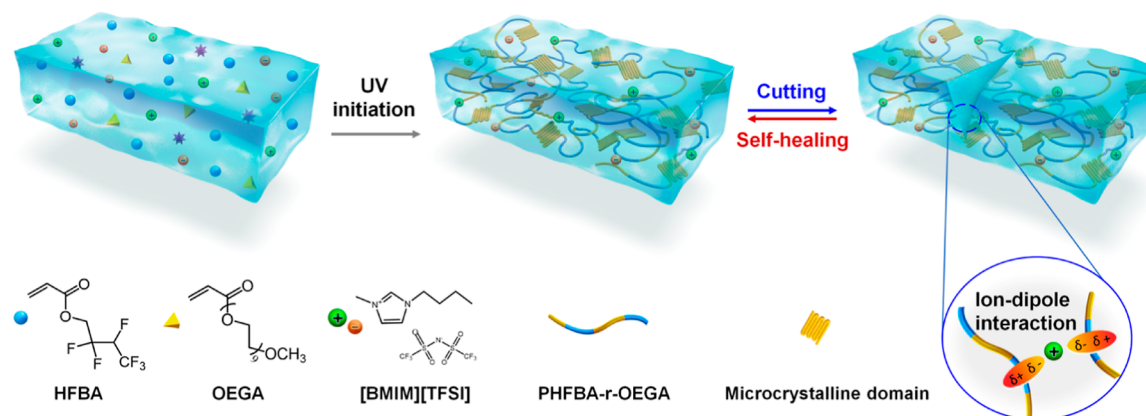


**Figure 1.** Schematic of the preparation process of SFCIs.

electronegative fluorine atoms and strong C–F bonds.<sup>29–31</sup> Among a variety of fluorinated polymers, thermoplastic polymers like polyvinylidene fluoride (PVDF) and poly(vinylidene fluoride-*co*-hexafluoropropylene) (PVDF-*co*-HFP) are commonly used due to their electroactivity and easy processibility. Nevertheless, the rigid crystalline regions among PVDF lead to poor deformation-tolerant and self-healing performance, severely reducing the durability and reliability of the resultant ionogels.<sup>31,32</sup> Furthermore, the improvements in the stretchability of ionogels have been achieved through increasing the loading of ILs, but this will undoubtedly result in the leakage of ILs. Therefore, the achievement of fluorinated ionogels with ultrastretchability, solvent-retention capacity, fast self-healability, and waterproofness is greatly desired for next-generation i-skins.

Herein, a semicrystalline fluorinated copolymer ionogel (SFCI) with extremely high stretchability, underwater stability, and fast self-healability was prepared by enriching hydrophobic ILs ([BMIM][TFSI]) in fluoroacrylate segment domains of the fluorinated copolymer matrix through ion–dipole interactions. The dense and reversible ion–dipole interactions imbued the SFCI with ultrastretchability (>6000%), fast self-healability (>96% healing efficiency after cutting and self-healing for 30 min), and solvent-retention capacity, while the physical cross-linking effects of semicrystalline oligoethylene glycol domains maintained their high mechanical strength (~251 kPa) and outstanding elasticity. Benefiting from the fluorinated copolymer matrix of PHFBA-r-OEGA and hydrophobic [BMIM][TFSI], the SFCI exhibited a high-temperature tolerance of up to 300 °C and unique waterproof performance. Moreover, the low freezing point of [BMIM][TFSI] allowed the SFCI to exhibit antifreezing performance at –35 °C. The SFCI also showed high transparency (>93% visible-light transmittance) due to the high compatibility of fluoroacrylate segments and [BMIM][TFSI]. Afterward, a skin-inspired sensor using the SFCI as a stretchable conductor was assembled, demonstrating high sensitivity (gauge factor: ~1) in a wide strain range of 0–200%, high durability with 1000 and 5000 cycles at 50 and 5% strains, respectively, fast response time within 0.3 s under 10% tensile strain, and unique waterproofness with stable response signals after immersion in water for various times in monitoring physiological signals of human motions.

## 2. EXPERIMENTAL SECTION

**2.1. Materials.** 2,2,3,4,4,4-Hexafluorobutyl acrylate (HFBA, >95%) was obtained from Aladdin Ltd. Oligoethylene glycol methyl ether acrylate (OEGA,  $M_w = \sim 481 \text{ g mol}^{-1}$ ) and 2,2-diethoxyacetophenone (DEAP, >95%) were purchased from TCI Chemicals. 1-Butyl-3-methylimidazolium bis((trifluoromethylsulfonyl)imide) ([BMIM][TFSI], 99%) was purchased from Adamas (Shanghai, China). All the chemicals were used without further purification.

**2.2. Preparations of SFCIs and PHFBA-r-OEGA.** Typically, HFBA and OEGA monomers, [BMIM][TFSI], and photoinitiators of DEAP were intensively mixed to obtain the homogeneous and transparent precursor solution. After being cast into a plastic mold, the solution was cured by an 8 W ultraviolet (UV) light (CL-1000L,  $\lambda = 365 \text{ nm}$ ) for 2 h. The molar ratio of HFBA and OEGA was fixed at 10/1. The SFCI-1, SFCI-2, SFCI-3, and SFCI-4 represent the as-prepared ionogels with IL/HFBA molar ratios of 1/9, 1/7, 1/5, and 1/3, respectively. The volume percentages of ILs in the four SFCI samples were 13, 16, 22, and 31%, respectively. The molar percentage of DEAP to the total monomers was set at 2% throughout the experiments. PHFBA-r-OEGA was prepared by photopolymerization of precursor solution of HFBA, OEGA, and DEAP without the addition of [BMIM][TFSI], while keeping other conditions similar to the SFCIs.

**2.3. Measurements of the SFCI Capacitance Sensor.** Capacitive strain sensing performance of SFCIs was measured on an LCR meter (TH2832) at an applied voltage of 1 V. The sensor was assembled with a dielectric layer (VHB 4910, 3M) sandwiched with two SFCI films ( $20 \times 10 \times 1 \text{ mm}^3$ ). Two copper wires were employed as the current collectors to connect the upper and lower surfaces of SFCI films. The other ends of copper wires were connected to the LCR meter. The stability and reliability of the SFCI sensor upon damages were tested at 25 °C. The humidity-dependent capacitive-type strain sensing performance of the SFCI-based sensors was performed at the 30 and 99% relative humidity (RH), respectively. To further confirm the waterproof performance of the SFCI-based strain sensor, its sensing performance after being stored in water for various times was measured. The SFCI-based strain sensors were attached to the prosthetic finger, elbow, and knee, as well as a dumbbell, to monitor complex human motions. The capacitance ( $C$ ) of the sensor was calculated by eq 1

$$C = \frac{\epsilon S}{4\pi k d} \quad (1)$$

where  $\epsilon$  is the dielectric constant of the dielectric layer,  $k$  is the electrostatic constant,  $S$  is the effective area of the two SFCI films, and  $d$  is the thickness of the dielectric layer.

The gauge factor (GF) was calculated by eq 2

$$\text{GF} = \frac{\Delta C/C_0}{\Delta \epsilon} \quad (2)$$

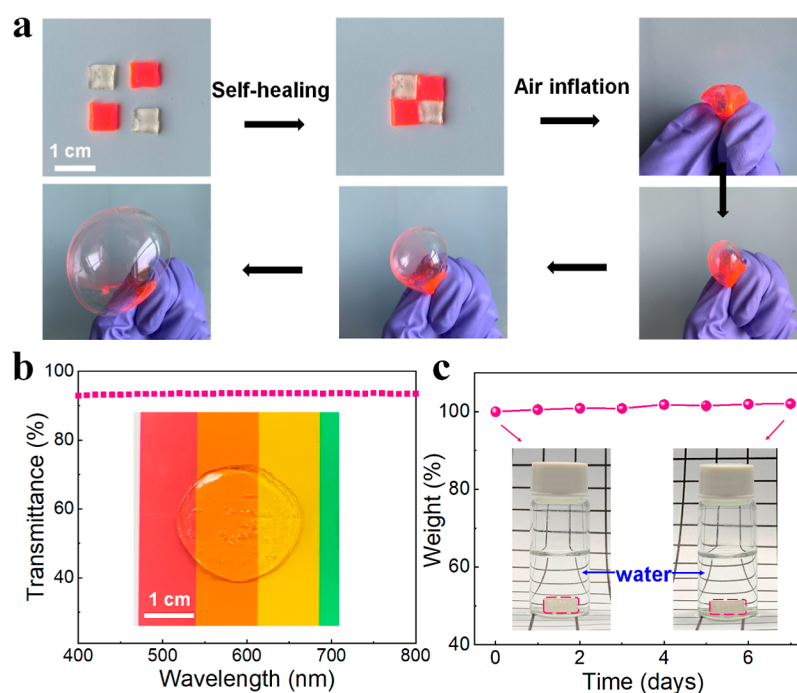


**Figure 2.** (a) Air inflation experiments of self-healed SFCI-2 film samples. Four square pieces were put together into contact, and the self-healed sample could be inflated into a balloon. (b) UV–vis spectra of a 0.2 mm thickness SFCI-2. The inset showing various colors could be seen clearly through the top of the SFCI-2 film. (c) Weight changes of SFCI-2 stored in water, demonstrating its waterproof performance. Insets showing that the underwater SFCI-2 sample maintained its original shape after 7 days.

where  $\Delta C$  is relative changes of the capacitance,  $C_0$  is the initial capacitance, and  $\Delta \epsilon$  is the change of strain.

### 3. RESULTS AND DISCUSSION

Figure 1 illustrates the preparation processes of the SFCI. Homogenous and transparent precursor solution containing HFBA, OEGA, [BMIM][TFSI], and DEAP was transferred into a PTFE mold and UV-photopolymerized to form a homogeneous film. The SFCI-1, SFCI-2, SFCI-3, and SFCI-4 represent the feeding molar ratios of [BMIM][TFSI] to HFBA of 1/9, 1/7, 1/5, and 1/3, respectively. The  $^1\text{H}$  nuclear magnetic resonance (NMR) spectroscopy of HFBA and OEGA monomers, as well as SFCI-2 under various photopolymerization time, was performed to investigate the polymerization rates of the two monomers within [BMIM][TFSI]. The  $^1\text{H}$  NMR spectra of hydrogen atoms among the acrylate double bonds of OEGA and HFBA showed peaks at 5.8–6.5 and 5.9–6.6 ppm (Figure S1), respectively. However, the peaks at 5.8–6.5 ppm disappeared in the  $^1\text{H}$  NMR spectrum of SFCI-2 after polymerizing for 30 min, indicating that the OEGA monomers were fully polymerized within the ILs. The HFBA monomers were completely consumed when prolonging the polymerization time to 60 min. The highly electronegative fluorine atoms in HFBA monomers affected their conversion during photopolymerization.<sup>33</sup>

Physically dual-cross-linked structures consisting of dense ion–dipole interactions between the fluoroacrylate segments and imidazolium cations of [BMIM][TFSI] as well as microcrystalline domains of POEGA were simultaneously achieved during the photopolymerization. The resulting SFCI samples exhibited incredible self-healability benefiting from reversible ion–dipole interactions.<sup>21,34</sup> As shown in Figure 2a, four square-shaped SFCI-2 film samples were put together into contact and self-healed into a complete film in

few seconds ( $<10$  s) at 25 °C, and the resultant self-healed film was successfully inflated to a large balloon without bursting (Movie S1).

High compatibility of the polymer matrix with ILs is essential for preparing ionogels with high transparency, and thus, [BMIM][TFSI], a fluorine-rich IL with high hydrophobicity, was selected for incorporating it into the fluoroacrylate segment domains of the fluorinated copolymer matrix. Figure 2b shows that the 0.2 mm thickness SFCI-2 film exhibited high transparency ( $>93\%$  visible-light transmittance). Elemental mapping images of fracture surface SFCI-2 samples (Figure S2) indicated that the C, N, O, F, and S elements were evenly distributed within the SFCI-2, further confirming the high compatibility between the PHFBA-r-OEGA backbone and fluorine-rich ILs. After the successful fabrication of SFCIs with high transparency, another kind of imidazolium-based fluoride-free IL, 1-butyl-3-methylimidazolium chloride ([BMIM]Cl), was substituted for [BMIM][TFSI] for the preparation of ionogels. As shown in Figure S3, the resulting [BMIM][Cl]-based ionogel was opaque, which was ascribed to the poor compatibility between the fluoride-free ILs and fluoroacrylate segments. Thus, we chose [BMIM][TFSI] as the representative IL owing to its fluorine-rich feature of high compatibility with fluoroacrylate segments.

Contact angle tests were performed to evaluate the hydrophobicity of the surface of PHFBA-r-OEGA and SFCIs (Figure S4). The contact angles of a water droplet on PHFBA-r-OEGA were measured to be  $98 \pm 4.0^\circ$ . The contact angles of SFCI-1, SFCI-2, SFCI-3, and SFCI-4 were calculated as  $116 \pm 3.1$ ,  $118 \pm 2.4$ ,  $119 \pm 2.5$ , and  $120 \pm 2.2^\circ$ , respectively. The contact angles of SFCIs gradually increased when the fluorine-rich [BMIM][TFSI] content increased, confirming a hydrophobic nature of SFCIs. The high hydrophobicity of SFCIs was originated from the fluorinated copolymer matrix and the

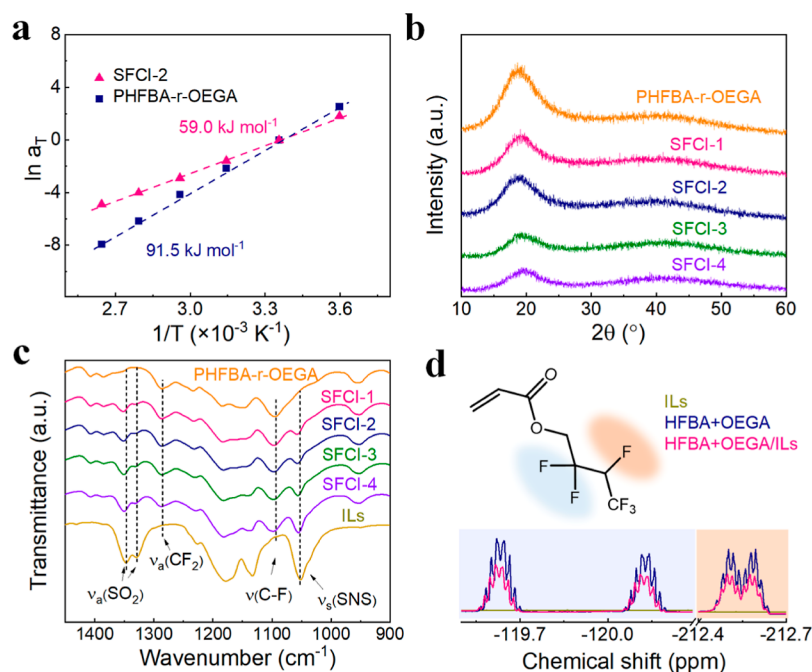


**Figure 3.** Compositional and structural characterizations. (a) Activation energy derived from Arrhenius plots for shift factors of SFCI-2 and PHFBA-r-OEGA. (b) XRD patterns of PHFBA-r-OEGA and SFCIs. (c) ATR-FTIR spectra of PHFBA-r-OEGA, SFCIs, and ILs. (d)  $^{19}\text{F}$  NMR spectra of model samples of ILs, HFBA + OEGA, and HFBA + OEGA/ILs in  $\text{CDCl}_3$ .

fluorine-rich ILs. Swelling measurements were performed to evaluate the waterproof performance of SFCIs. As shown in Figure 2c, the weight and shape of SFCI-2 were almost unchanged when stored in water during testing, demonstrating its outstanding waterproofness. The unique waterproof performance made the SFCIs promising to readily work as an emerging waterproof wearable sensor. Moreover, the as-prepared SFCIs exhibited high ionic conductivities at room temperature, and the ionic conductivities of SFCIs ranged from  $8.89 \times 10^{-4}$  to  $2.42 \times 10^{-2} \text{ S m}^{-1}$  with the increasing content of the fluorine-rich ILs (Figure S5). The SFCI-2 maintained stable ionic conductivities at  $25^\circ\text{C}$  for over 7 days (Figure S6). The ionic conductivity of SFCI-2 increased from  $2.67 \times 10^{-3}$  to  $0.26 \text{ S m}^{-1}$  in the temperature range of  $25$ – $200^\circ\text{C}$  (Figure S7), which is attributed to the fact that higher temperatures contributed to faster movements of ions within the polymer matrix, easier ion transport, and higher ionic conductivity.

X-ray photoelectron spectroscopy (XPS) was conducted to evaluate surface elemental compositions of PHFBA-r-OEGA and SFCI-2. XPS spectra of the abovementioned two samples (Figure S8a) showed similar characteristic peaks of fluorine ( $\sim 835$  and  $690 \text{ eV}$  for F KLL and F 1s), oxygen ( $\sim 531 \text{ eV}$  for O 1s), and carbon ( $\sim 285 \text{ eV}$  for C 1s). Upon the addition of fluorine-rich [BMIM][TFSI], N 1s and S 2p spectra in the SFCI-2 were introduced. The N 1s spectra can be deconvoluted into two peaks centered at  $400.7$  and  $398.1 \text{ eV}$  (Figure S8b), corresponding to the N atoms in  $\text{N}^+$  of imidazole rings<sup>4,35,36</sup> and S–N–S of anions of fluorine-rich ILs,<sup>37</sup> respectively. Also, the S 2p spectra attributed to fluorine-rich ILs were deconvoluted into  $2p_{1/2}$  and  $2p_{3/2}$  peaks (Figure S8c). Rheological tests were performed to investigate the ion–dipole interactions within the SFCI-2. The master curves of PHFBA-r-OEGA and SFCI-2 were recorded at a reference temperature of  $25^\circ\text{C}$  using the time–temperature superposition principle via oscillatory frequency sweep tests (Figure S9). The apparent activation energy ( $E_a$ ) of PHFBA-r-OEGA was estimated by

the Arrhenius equation ( $E_a$  of  $91.5 \text{ kJ mol}^{-1}$ ) with the frequency-scale shift factor ( $\alpha_T$ ). With the incorporation of the fluorine-rich ILs, the ion–dipole interaction within the SFCI-2 was observed. The  $E_a$  of SFCI-2 was measured to be  $59.0 \text{ kJ mol}^{-1}$ , and the relatively low  $E_a$  not only decreased the energy barriers of PHFBA-r-OEGA but also promoted the segmental motions (Figure 3a). These results clearly explained that the SFCI-2 had extremely fast self-healability.

The chemical and crystalline structures of SFCIs were further investigated by X-ray diffraction (XRD), attenuated total reflection Fourier transformed infrared spectroscopy (ATR-FTIR), and  $^{19}\text{F}$  NMR. The XRD patterns from PHFBA-r-OEGA and SFCIs showed diffraction peaks located at  $2\theta = \sim 20^\circ$  (Figure 3b), corresponding to the microcrystalline of ether segments.<sup>38</sup> The crystallinity of PHFBA-r-OEGA that was calculated from XRD patterns was 43.0%. A significant decrease from 38.4 to 19.8% in the crystallinity of SFCIs with the increasing content of fluorine-rich ILs was observed (Table S1), revealing the plasticizing effects of ILs on the copolymer matrix. Furthermore, the ion–dipole interactions between PHFBA-r-OEGA and fluorine-rich ILs were identified by FTIR. Figure 3c and Table S2 show that the FTIR peaks at  $1286 \text{ cm}^{-1}$  ( $\text{C-F}_2$  antisymmetric stretching vibration)<sup>21</sup> and  $1095 \text{ cm}^{-1}$  ( $\text{C-F}$  stretching vibration)<sup>39</sup> in the PHFBA-r-OEGA shifted to relatively high wavenumbers with the addition of the fluorine-rich ILs. Meanwhile, three distinct peaks at  $1348$  and  $1330 \text{ cm}^{-1}$  ( $\text{SO}_2$  antisymmetric stretching vibrations) and  $1052 \text{ cm}^{-1}$  (SNS antisymmetric stretching vibration) observed in the fluorine-rich ILs also shifted to relatively high wavenumbers, revealing that the electron cloud density around the  $\text{TFSI}^-$  increased, as imidazolium cations were pulled away by F atoms.<sup>40</sup> These results indicated the formation of ion–dipole interactions between the F atoms of PHFBA-r-OEGA and the imidazolium cations of [BMIM][TFSI].  $^{19}\text{F}$  NMR results are shown in Figure 3d, demonstrating that the peaks of F atoms in HFBA moved

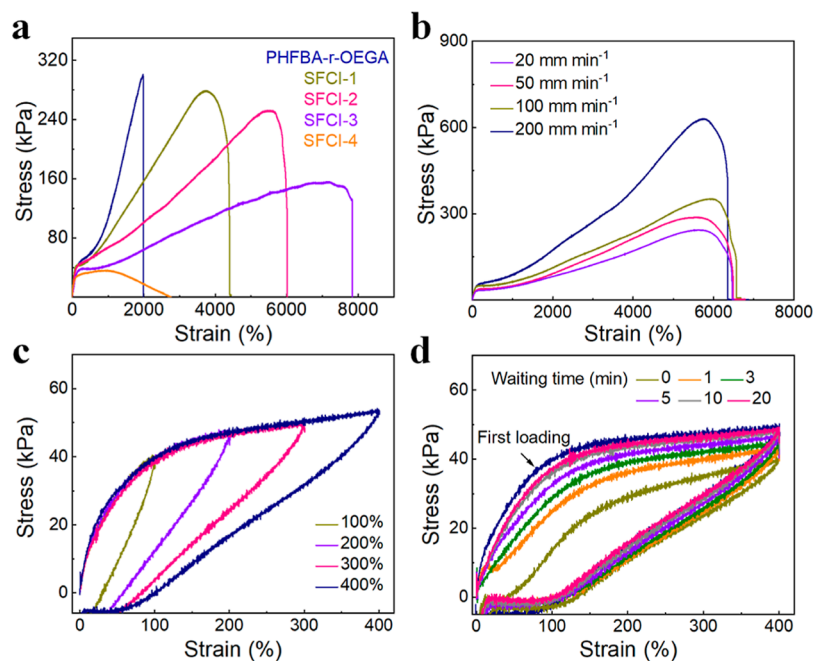
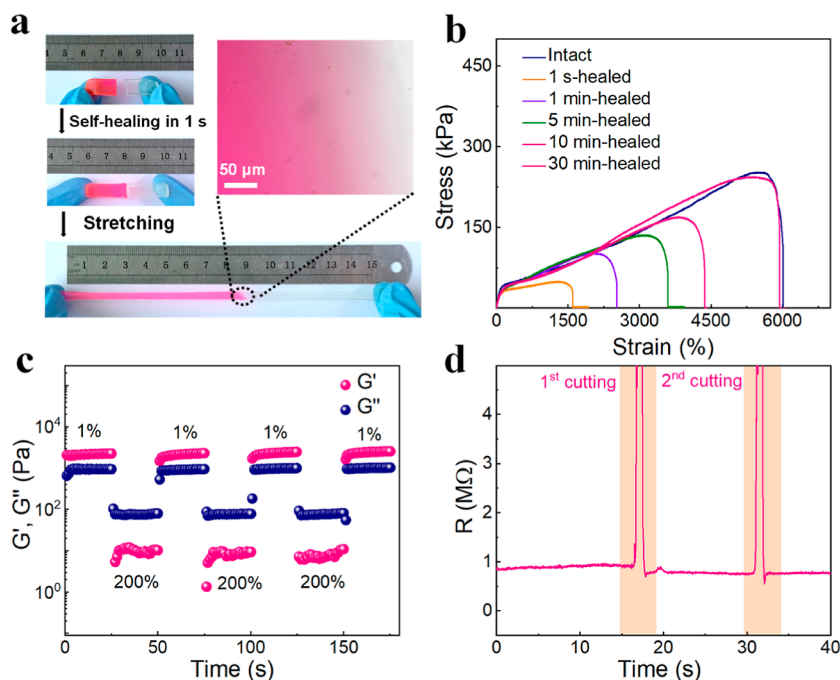


**Figure 4.** Mechanical performance. (a) Typical tensile stress–strain curves of PHFBA-r-OEGA and SFCIs at a stretching rate of 50 mm min<sup>-1</sup>. (b) Tensile stress–strain curves of SFCI-2 at varied strain rates. (c) Cyclic stress–strain curves of SFCI-2 under varied strains. The stretching rate was set at 50 mm min<sup>-1</sup>. (d) Recovery of SFCI-2 for different waiting times.

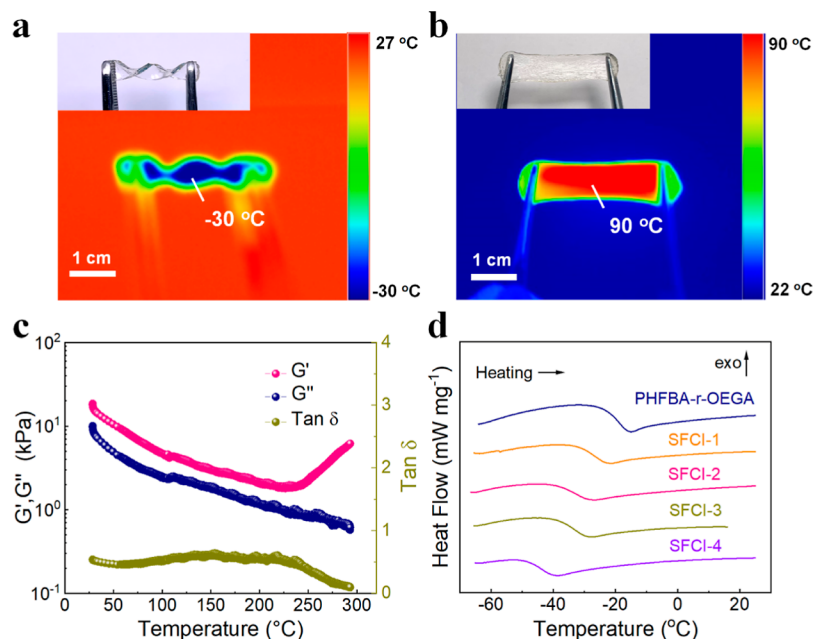
toward relatively low field with the addition of [BMIM][TFSI] and the corresponding intensity decreased, further confirming the presence of ion–dipole interactions. Moreover, scanning electron microscopy (SEM) was carried out to investigate the influence of physically dual-cross-linked interactions on the structure of SFCIs. Figure S10 shows the cross-sectional SEM images of SFCI samples after solvent exchange and freeze-drying. The SFCI-1 with a small amount of ILs presented nonuniform pore size distributions because the fluorine-rich ILs hardly enriched strong semicrystalline domains. When the content of fluorine-rich ILs was relatively high in the SFCI-4, the pore size significantly decreased and the distribution became uniform and ordered due to the increase of relatively weak and dense ion–dipole interactions.

Figure S11 shows typical tensile stress–strain curves of PHFBA, POEGA, and PHFBA-r-OEGA. Compared with those of PHFBA and POEGA, the mechanical strength and toughness of PHFBA-r-OEGA were enhanced incredibly. By tuning the molar ratio of fluorine-rich ILs and HFBA, a series of SFCIs with distinct mechanical properties were achieved. As shown in Figure 4a and summarized in Table S3, the rigid microcrystalline domains led to low stretchability and high mechanical strength of PHFBA-r-OEGA without the addition of fluorine-rich ILs.<sup>41</sup> When the IL/HFBA molar ratios increased from 1/9 to 1/5, the stretchability of SFCIs significantly enhanced from 1980 to 7840%, while the toughness increased from 2.6 to 8.0 MJ m<sup>3</sup>, respectively. However, the further increase of the molar ratio of IL/HFBA to 1/3 decreased the stretchability and mechanical strength of SFCIs. It is because the higher content of ILs resulted in lower crystallinity and entanglement of polymer chains in SFCIs. Furthermore, the SFCI-2 exhibited a high mechanical strength (~251 kPa) and a high stretchability (>6000%) (Movie S2), which was a record-high stretchability among the reported ionic conductors in the literature.<sup>34,42–46</sup>

The deformation-rate dependence of tensile behaviors further confirmed the dynamic and reversible features of ion–dipole interactions. Figures 4b and S12 show that the mechanical strength of SFCI-2 increased pronouncedly from 251 to 630 kPa, accompanied by the increased deformation rates. However, the fracture strain of SFCI-2 was independent of the deformation rate, even the deformation rate was up to 200 mm min<sup>-1</sup>, indicating that few strong interactions (i.e., microcrystalline domains) had been broken before the full breakage of relatively weak ion–dipole interactions.<sup>47</sup> Moreover, the elasticity and dissipative capacity of SFCI-2 was assessed by cyclic tensile tests. In Figure 4c, the SFCI-2 showed pronounced hysteresis and relatively small plastic deformation. The area of hysteresis loops gradually increased with increasing cyclic strains, revealing that the SFCI-2 could effectively dissipate energy through the breakage of ion–dipole bonds. However, when the SFCI-2 was stretched and released successively, Young's modulus and strength of the next cycle were lower than that of the previous cycle (Figure S13), which was attributed to the fact that a sliding mechanism based on dynamic bonds required enough time for the recovery of mechanical properties.<sup>48</sup> To confirm the self-recovery capability of SFCI-2 under different waiting times, cyclic tensile tests were carried out under a loading strain of 400% (Figure 4d). It was surprising that the short waiting time of 1 min contributed to a 70% recovery of the hysteresis ratio (area ratio of the second hysteresis loop to the first) (Figure S14).<sup>49</sup> The residual strain decreased with the increasing waiting time and disappeared after the waiting time of 20 min, which meant that the plastic deformation was fully removed. In striking contrast to stretchable ionic conductors in the literature (Table S4),<sup>34,49–52</sup> the SFCI-2 showed a small residual strain after unloading and a rapid self-recovery capability with a large recovery of the hysteresis ratio in short waiting time during the second loading/unloading cycle.



**Figure 5.** Self-healing performance. (a) Photographs showing the self-healing ability of SFCI-2. The inset showing an optical microscopy image of the healed area of SFCI-2. (b) Stress–strain curves of the pristine and healed SFCI-2 sample after various healing times. (c) Alternate step strain sweep tests with alternating shear strains of 1 and 200% with 25 s for SFCI-2. (d) Recovery of ionic conductivity of SFCI-2 upon two cutting and self-healing cycles.



**Figure 6.** Extreme-temperature tolerance. Optical images and corresponding thermal images of SFCI-2 at (a)  $-30$  and (b)  $90$   $^{\circ}\text{C}$ , respectively. (c) DMA curves of SFCI-2 from 25 to  $300$   $^{\circ}\text{C}$ . (d) DSC thermograms of PHFBA-r-OEGA and SFCIs from  $-70$  to  $25$   $^{\circ}\text{C}$ .

The dynamic and reversible features of ion–dipole interactions imbued SFCIs with ultrafast self-healability at room temperature. To make the cut region more distinguishable, one of the SFCI-2 samples was colored by rhodamine B (red). Subsequently, two SFCI samples with different colors were cut into half and gently put together into contact for self-healing in only 1 s (Figure 5a). It was noteworthy that the repaired sample was capable of withstanding large stretching deformation and the crack between two fractured SFCI-2

samples was almost invisible. To determine the self-healing efficiency of fractured SFCI samples more accurately, tensile tests before and after self-healing processes were carried out. Figure 5b shows tensile stress–strain curves of the self-healed SFCI-2 samples under various healing times (1 s, 1 min, 5 min, 10 min, and 30 min). Surprisingly, the fracture strain of the healed SFCI-2 was more than 1500% after self-healing in only 1 s (Movie S3). Moreover, the fracture strain and mechanical strength of the as-healed samples were restored to 98.9 and

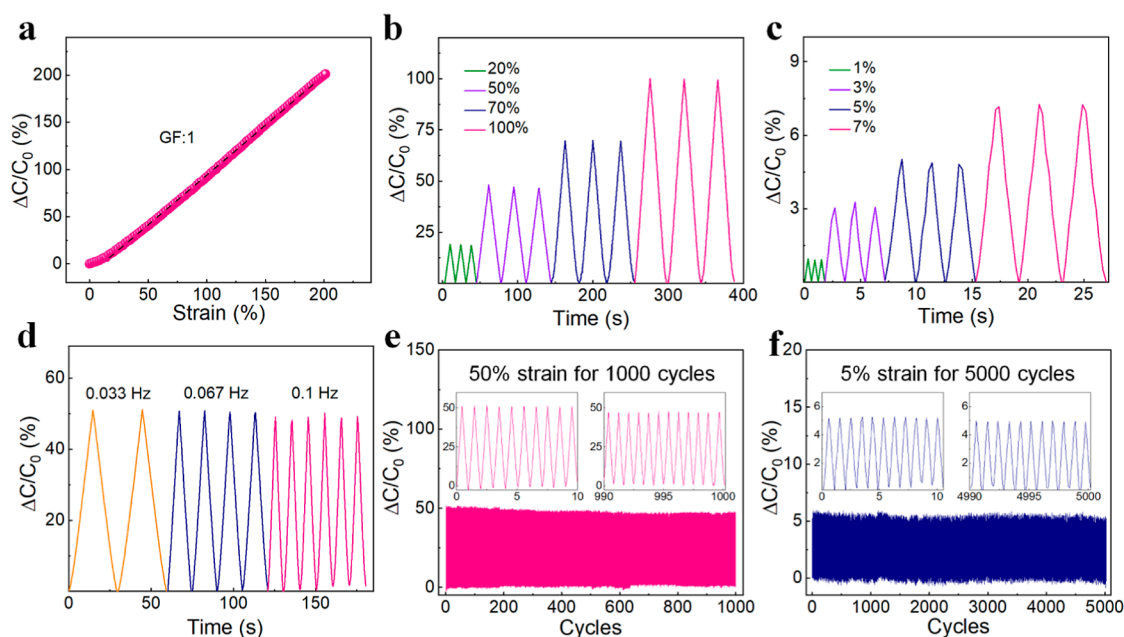


**Figure 7.** Capacitive sensing performance of the SFCI sensor. (a) Relative capacitance variations as a function of strain. Relative capacitance variations (b) under large strains (20, 50, 70, and 100%) and (c) under small strains (1, 3, 5, and 7%). (d) Relative capacitance variations at various loading frequencies upon stretching to 50% strain. Cyclic stability tests under (e) 50% strain for 1000 cycles and (f) 5% strain for 5000 cycles.

96.7% of those before cutting after healing for 30 min (Figure S15), respectively. To further illustrate the self-healing performance of the SFCI after multiple cutting and self-healing cycles, the tensile stress–strain curves of the cut and self-healed SFCI-2 samples are shown in Figure S16. The elastic modulus and toughness of the self-healed SFCI-2 samples merely declined slightly after cutting and self-healing three times, further indicating the excellent self-healing ability of the as-obtained SFCI.

The self-healability of SFCIs was further confirmed by rheological measurements. Strain amplitude sweep tests of SFCI-2 are shown in Figure S17. The storage moduli ( $G'$ ) of SFCI-2 were much higher than the loss moduli ( $G''$ ) at a small shear strain (<10%), indicating its solid-like elasticity behavior.<sup>53–56</sup> The  $G'$  values of SFCI-2 began to decrease and the  $G''$  values became higher than the  $G'$  values at a large shear strain (>100%), revealing that the physically cross-linked network was damaged at a large strain.<sup>57</sup> Cyclic step-strain sweep tests with an alternate small shear strain of 1% and large shear strain of 200% were performed (Figure 5c). At the shear strain of 1%, the  $G'$  value was higher than that of  $G''$ . However, when the shear strains grew to 200%, the  $G'$  values underwent a dramatic decline and were lower than that of  $G''$ . Notably, the  $G'$  and  $G''$  values of SFCI-2 instantly recovered to their initial values after the shear strain returned to 1%.<sup>43</sup> Moreover, the self-healing capacity of the ion conductivity of SFCI-2 is shown in Figure 5d, and the resistances were recovered to its original value in short time after two cutting–healing cycles.<sup>58</sup>

Owing to the low freezing point and negligible vapor pressure of [BMIM][TFSI],<sup>43</sup> the SFCIs exhibited outstanding stability under extreme environmental conditions of high and low temperatures. The mechanical flexibility of SFCI-2 under extreme temperature conditions is shown in Figure 6a,b, demonstrating that the SFCI-2 was capable of being twisted at  $-30$  °C and stretched at  $90$  °C, respectively. To explore the thermal limits of high-temperature environments for SFCI-2, dynamic thermomechanical analysis (DMA) measurements

were performed from 25 to 300 °C (Figure 6c). The  $G'$  values of SFCI-2 were higher than  $G''$  values even the temperature was up to 300 °C, indicating that the SFCI-2 exhibited outstanding elasticity behaviors under extremely high temperatures. The high-temperature tolerance of SFCI-2 was originated from the fluorinated PHFBA-r-OEGA backbone and the high thermal stability of [BMIM][TFSI]. Moreover, a gradual increase in the  $G'$  values of SFCI-2 with the temperature rising from 230 to 300 °C was attributed to the increase of cross-linking density caused by the oxidative cross-linking of polymer chains under such high temperatures.

To evaluate the antifreezing performance of SFCIs, glass transition temperatures ( $T_g$ ) of PHFBA-r-OEGA and SFCIs were measured by differential scanning calorimetry (DSC). The  $T_g$  of SFCIs was determined by the PHFBA-r-OEGA backbone and the fluorine-rich ILs because SFCIs only consisted of the abovementioned two components. PHFBA-r-OEGA had a  $T_g$  of  $-20.8$  °C (Figure 6d), whereas the  $T_g$  of the fluorine-rich ILs was about  $-84.0$  °C.<sup>59</sup> The  $T_g$  of SFCIs decreased from  $-20.8$  to  $-45.3$  °C with the increasing content of the fluorine-rich ILs, indicating the plasticizing effect of ILs on PHFBA-r-OEGA, which was consistent with the abovementioned XRD results. The decrease of  $T_g$  contributed to the mobility of polymer chains, promoting the self-healability of SFCIs.<sup>60</sup> In addition to the freeze-resistant performance, the thermal stability of SFCIs was assessed using thermogravimetric analysis (TGA). In Figure S18a, the SFCIs showed high decomposition temperatures at  $\sim 300$  °C under a nitrogen atmosphere. To further demonstrate the long-term thermal stability, the weight loss of SFCI-2 stored at 100 °C was measured for 48 h (Figure S18b). The weight of SFCI-2 maintained stability due to the dense ion–dipole interactions of [BMIM][TFSI] with the polymer matrix, which effectively prevented the evaporation of ILs. In short, SFCIs exhibited excellent heat/freeze-resistant performance, revealing their excellent stability in a wide operating temperature range.

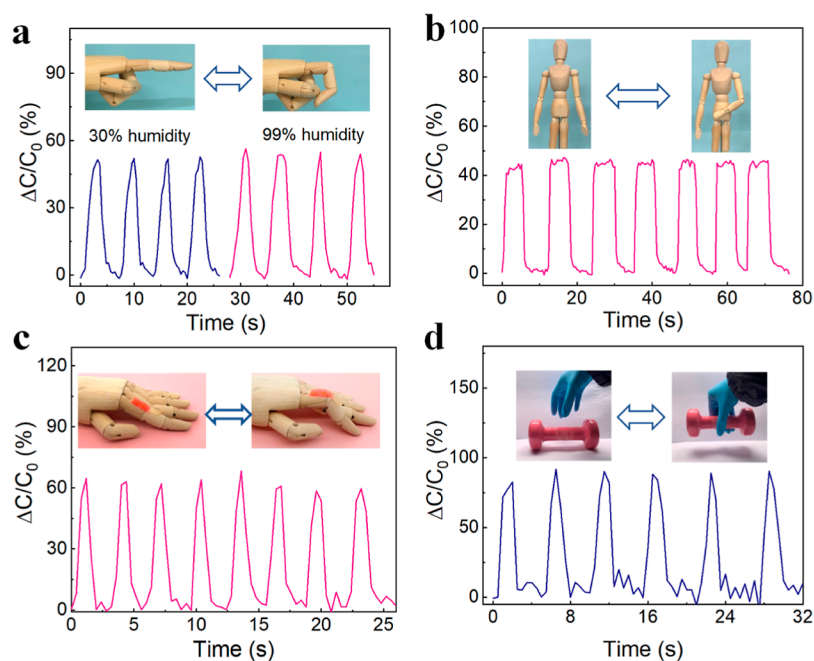


**Figure 8.** Wearable SFCI capacitance sensor detecting complex mechanical motions. Relative capacitance variations of the sensor monitoring (a) prosthetic finger bending under varied humidity environments, (b) prosthetic elbow bending, (c) prosthetic finger bending upon cutting and self-healing, and (d) dumbbell lifting.

Besides, it is also important for ionic conductors to have a stable and wide electrochemical window, which meets the voltage demands of most electronic devices (e.g., lithium–sulfur batteries, lithium–nickel–manganese–cobalt oxide batteries, and supercapacitors). Linear sweep voltammetry tests were performed to measure the decomposition voltage of SFCIs at a scan rate of  $1 \text{ mV s}^{-1}$  from 0 to 6 V. Owing to the well-known high electrochemical stability of ILs, the SFCI-2 exhibited a high decomposition voltage at  $\sim 3.6 \text{ V}$  (Figure S19), which was much higher than those of hydrogel electrolytes (decomposition voltage of  $< 1.0 \text{ V}$ ).<sup>5,61,62</sup> Moreover, squeezing tests were measured to assess the capability of IL retentions in the SFCI (Figure S20). There was no leaked [BMIM][TFSI] on the weighing paper when squeezing the SFCI-2 sample, indicating that the strong ion–dipole interaction contributed to preventing any leakage of ILs.

As summarized in Table S5, the SFCI exhibited not only a high mechanical strength of 251 kPa but also an ultra-stretchability up to 6000%, which was a record-high stretchability among the reported ionogels in the literature. The SFCI was able to self-heal rapidly with a 96% healing efficiency after cutting and self-healing for 30 min. The waterproofness of the SFCI was fascinating, which contributed to the long-term application of the SFCI sensor in high humidity conditions. The intriguing properties with high elongation at break, ultrafast self-healability, and waterproofness of the SFCI are promising as an ionic conductor for assembling skin-inspired capacitance sensors (Figure S21).<sup>5,15,34,62–64</sup> In Figure S22, the SFCI sensor was constructed by integrating two SFCI films with a dielectric layer (VHB 4910, 3M), and the upper and lower SFCI films were connected to two copper current collectors. When the SFCI sensor was subjected to an external force, both the effective area ( $S$ ) of the SFCI and the thickness ( $d$ ) of the dielectric layer changed, resulting in the capacitance variations of the SFCI sensor.<sup>65</sup> In Figure 7a, the SFCI sensor presented

a large-strain responsive range from 0 to 200% strain, and its gauge factor (GF) was calculated to be 1, which was consistent with the theoretical prediction.<sup>11</sup> Figure 7b,c shows the evolutions of the relative capacitance variation ( $\Delta C/C_0$ ) signals of the sensor during the successive stretching/releasing cycles at large strains (20, 50, 70, and 100%) and small strains (1, 3, 5, and 7%), respectively. Repeatable and strain-dependent capacitance signals were observed, indicating the ability of the sensor in discerning deformation degrees. In Figure 7d, even under frequency ranging from 0.033 to 0.1 Hz, stable and continuous capacitance responses upon 50% strain were demonstrated, revealing potentials of SFCI sensors for detecting dynamic strains. The SFCI-2-based strain sensor also exhibited fast response time ( $\sim 0.3 \text{ s}$ ) and recovery time ( $\sim 0.6 \text{ s}$ ) under 10% tensile strain due to its outstanding elasticity (Figure S23).

To test the durability of the SFCI sensor for long-term applications, the SFCI sensor was stretched to 50% strain for 1000 cycles and 5% strain for 5000 cycles, respectively. In Figure 7e,f, highly stable and reproducible capacitance signals were observed, showing an excellent reliability of the SFCI sensor during long-term stretching/releasing cycles. The wearable SFCI capacitance sensor was used to monitor diverse motions of the finger, elbow, and knee bendings. Figure 8a shows that the SFCI-2-based sensor was utilized to detect the prosthetic finger straightening/bending processes at 30 and 99% RH, respectively. The  $\Delta C/C_0$  signals remained almost unchanged for four cycles under different humidity conditions, suggesting the humidity-independent sensing performance of the SFCI sensor. Furthermore, the SFCI sensor was immersed in large amounts of water for various times (0, 12, and 24 h) to demonstrate its waterproof performance. The sensing performance of the SFCI sensor monitoring the prosthetic knee bending is shown in Figure S24, indicating the high stability of the SFCI sensor even after long-term immersion in water. This was because the integration of the fluorinated copolymer

matrix and fluorine-rich ILs enabled the SFCI sensor with excellent waterproof performance. Figure 8b shows that the SFCI sensor was also capable of monitoring the prosthetic elbow bending motions, and the  $\Delta C/C_0$  signals were kept steadily. In addition, the stability and reliability of the SFCI sensor under damaged conditions were assessed. Figure 8c shows the  $\Delta C/C_0$  signals of the capacitance sensor assembled by the self-healed SFCI samples during continuous finger straightening/bending cycles. Repeatable and reliable capacitance signals were observed, further indicating the high durability and stability of the SFCI sensor. Moreover, the SFCI sensor could perceive different dynamic pressures and real-time generate continuous and stable  $\Delta C/C_0$  signals (Figure S25). The SFCI sensor was attached to the side of a dumbbell, and the processes of the dumbbell lifted/fallen by a volunteer caused fully repeatable capacitance variations (Figure 8d).

#### 4. CONCLUSIONS

In summary, we developed a SFCI by selectively enriching hydrophobic ILs of [BMIM][TFSI] in fluoroacrylate segment domains of the fluorinated copolymer matrix through ion–dipole interactions. Owing to the presence of reversible and dense ion–dipole interactions between the imidazolium cations of [BMIM][TFSI] and fluoroacrylate segments, the SFCI exhibited ultrastretchability (>6000%), fast self-healability at room temperature, and solvent-retention capacity. Meanwhile, the stiff microcrystalline domains enabled the SFCI with high mechanical strength (~251 kPa) and outstanding reversible elasticity. The SFCI exhibited waterproof performance due to the presence of both the hydrophobic [BMIM][TFSI] and fluorinated copolymer matrix of PHFBA-r-OEGA, which effectively prevented hygroscopicity of ionogels in humid environments. The SFCI also showed high-temperature tolerance up to 300 °C and freeze-resistant performance as low as –35 °C. Owing to the high compatibility of the fluoroacrylate chain and [BMIM]-[TFSI], the SFCI was highly transparent (>93% visible-light transmittance). The versatile design and impressive performance made SFCIs promising as highly waterproof and stretchable ionic conductors for wearable strain sensors with a high gauge factor of 1.0, linear response range of 0–200% strain, fast response time within 0.3 s under 10% tensile strain, stable response signals after immersion in water for various times (0, 12, and 24 h), and durability to 1000 and 5000 cycles at 50 and 5% strains, respectively, with great implication for exploring advanced wearable strain sensing applications in complex and extreme environments.

#### ■ ASSOCIATED CONTENT

##### Supporting Information

The Supporting Information is available free of charge at <https://pubs.acs.org/doi/10.1021/acsami.1c16081>.

Characterizations;  $^1\text{H}$  NMR spectra of the OEGA monomer, HFBA monomer, and SFCI-2 after various polymerization times; SEM image and elemental mapping images of SFCI-2; photograph of the [BMIM]-Cl-based ionogels; water contact angles of PHFBA-r-OEGA and SFCIs; ionic conductivities of SFCIs; ionic conductivities of SFCI-2 after storing for 7 days; temperature dependence of ionic conductivity of SFCI-2; XPS spectra of PHFBA-r-OEGA and SFCI-2;

frequency dependence of  $G'$ ,  $G''$ , and  $\text{Tan } \delta$  of PHFBA-r-OEGA and SFCI-2; SEM images of the treated SFCI-1 and SFCI-4; tensile stress–strain curves of PHFBA, POEGA, and PHFBA-r-OEGA; strain rate dependence of fracture stress and fracture strain of SFCI-2; cyclic stress–strain curves of SFCI-2; waiting time dependence of the residual strain and hysteresis ratio of SFCI-2; fracture mechanical strength and fracture strain of healed SFCI-2; tensile stress–strain curves of SFCI-2 after multiple cutting and self-healing cycles; oscillatory amplitude sweep tests at an angular frequency of  $5 \text{ rad s}^{-1}$  for SFCI-2; TGA curves of ILs, PHFBA-r-OEGA, and SFCIs; weight retention of SFCI-2 at 100 °C; decomposition voltage tests of SFCIs by linear sweep voltammetry; photographs showing the SFCI-2 film squeezed on a weighting paper; comparisons between SFCI-2 and previously reported ionic conductors; structure and circuit schematic illustration of the as-assembled capacitance sensor; response and recover time of the SFCI-2-based strain sensor; sensing performance of the SFCI-2-based strain sensor after immersion in water for various times; relative capacitance changes of the SFCI-2-based strain sensor at various pressures; tables summarizing crystallinity of PHFBA-r-OEGA and SFCIs calculated from XRD patterns, FTIR characteristic peaks in PHFBA-r-OEGA, SFCIs, and [BMIM][TFSI], mechanical properties of PHFBA-r-OEGA and SFCIs, comparisons of SFCI-2 and stretchable ionic conductors in the literature in terms of cyclic tensile strain, residual strain, recovery of hysteresis ratio, and waiting time during the second loading/unloading cycle, as well as mechanical properties, self-healing performance, and waterproofness of SFCI-2 and ionogels in the literature (PDF)

Fractured and self-healed SFCI inflating into a large balloon (AVI)

SFCI stretched to 6000% with 10× play speed (AVI)

Tensile performance of fractured SFCI after ultrafast self-healability with 10× play speed (AVI)

#### ■ AUTHOR INFORMATION

##### Corresponding Author

Chao Zhang – State Key Laboratory for Modification of Chemical Fibers and Polymer Materials, College of Materials Science and Engineering, Donghua University, Shanghai 201620, P. R. China; [orcid.org/0000-0003-1255-7183](https://orcid.org/0000-0003-1255-7183); Email: [czhang@dhu.edu.cn](mailto:czhang@dhu.edu.cn)

##### Authors

Peiru Shi – State Key Laboratory for Modification of Chemical Fibers and Polymer Materials, College of Materials Science and Engineering, Donghua University, Shanghai 201620, P. R. China

Yufeng Wang – State Key Laboratory for Modification of Chemical Fibers and Polymer Materials, College of Materials Science and Engineering, Donghua University, Shanghai 201620, P. R. China

Weng Wee Tjiu – Institute of Materials Research and Engineering, Agency for Science, Technology and Research (A\*STAR), Singapore 138634, Singapore

Tianxi Liu – State Key Laboratory for Modification of Chemical Fibers and Polymer Materials, College of Materials Science and Engineering, Donghua University, Shanghai

201620, P. R. China; Key Laboratory of Synthetic and Biological Colloids, Ministry of Education, School of Chemical and Material Engineering, Jiangnan University, Wuxi 214122, P. R. China; [orcid.org/0000-0002-5592-7386](https://orcid.org/0000-0002-5592-7386)

Complete contact information is available at:  
<https://pubs.acs.org/10.1021/acsami.1c16081>

### Author Contributions

The manuscript was written through contributions of all the authors. All the authors have given approval to the final version of the manuscript.

### Notes

The authors declare no competing financial interest.

### ACKNOWLEDGMENTS

This work was supported by the National Natural Science Foundation of China (grant nos. 52122303 and 21875033).

### REFERENCES

- (1) Ji, S.; Wan, C.; Wang, T.; Li, Q.; Chen, G.; Wang, J.; Liu, Z.; Yang, H.; Liu, X.; Chen, X. Water-Resistant Conformal Hybrid Electrodes for Aquatic Endurable Electrocardiographic Monitoring. *Adv. Mater.* **2020**, *32*, 2001496.
- (2) Zhang, C.; Zhou, Y.; Han, H.; Zheng, H.; Xu, W.; Wang, Z. Dopamine-Triggered Hydrogels with High Transparency, Self-Adhesion, and Thermoresponse as Skinlike Sensors. *ACS Nano* **2021**, *15*, 1785–1794.
- (3) Wang, S.; Xu, J.; Wang, W.; Wang, G.-J. N.; Rastak, R.; Molina-Lopez, F.; Chung, J. W.; Niu, S.; Feig, V. R.; Lopez, J.; Lei, T.; Kwon, S.-K.; Kim, Y.; Foudeh, A. M.; Ehrlich, A.; Gasperini, A.; Yun, Y.; Murmann, B.; Tok, J. B.-H.; Bao, Z. Skin Electronics from Scalable Fabrication of an Intrinsically Stretchable Transistor Array. *Nature* **2018**, *555*, 83–88.
- (4) Ren, Y.; Liu, Z.; Jin, G.; Yang, M.; Shao, Y.; Li, W.; Wu, Y.; Liu, L.; Yan, F. Electric-Field-Induced Gradient Ionogels for Highly Sensitive, Broad-Range-Response, and Freeze/Heat-Resistant Ionic Fingers. *Adv. Mater.* **2021**, *33*, 2008486.
- (5) Ren, Y.; Guo, J.; Liu, Z.; Sun, Z.; Wu, Y.; Liu, L.; Yan, F. Ionic Liquid-Based Click-Ionogels. *Sci. Adv.* **2019**, *5*, No. eaax0648.
- (6) Keplinger, C.; Sun, J.-Y.; Foo, C. C.; Rothmund, P.; Whitesides, G. M.; Suo, Z. Stretchable, Transparent, Ionic Conductors. *Science* **2013**, *341*, 984.
- (7) Xie, Z.; Avila, R.; Huang, Y.; Rogers, J. A. Flexible and Stretchable Antennas for Biointegrated Electronics. *Adv. Mater.* **2020**, *32*, 1902767.
- (8) Matsuhisa, N.; Chen, X.; Bao, Z.; Someya, T. Materials and Structural Designs of Stretchable Conductors. *Chem. Soc. Rev.* **2019**, *48*, 2946–2966.
- (9) Hu, C.; Zhang, Y.; Wang, X.; Xing, L.; Shi, L.; Ran, R. Stable, Strain-Sensitive Conductive Hydrogel with Antifreezing Capability, Remoldability, and Reusability. *ACS Appl. Mater. Interfaces* **2018**, *10*, 44000–44010.
- (10) Peng, Q.; Chen, J.; Wang, T.; Peng, X.; Liu, J.; Wang, X.; Wang, J.; Zeng, H. Recent Advances in Designing Conductive Hydrogels for Flexible Electronics. *InfoMat* **2020**, *2*, 843–865.
- (11) Sun, J.-Y.; Keplinger, C.; Whitesides, G. M.; Suo, Z. Ionic Skin. *Adv. Mater.* **2014**, *26*, 7608–7614.
- (12) Lei, Z.; Wu, P. A Supramolecular Biomimetic Skin Combining a Wide Spectrum of Mechanical Properties and Multiple Sensory Capabilities. *Nat. Commun.* **2018**, *9*, 1134.
- (13) Xiang, S.; Zheng, F.; Chen, S.; Lu, Q. Self-Healable, Recyclable, and Ultrastrong Adhesive Ionogel for Multifunctional Strain Sensor. *ACS Appl. Mater. Interfaces* **2021**, *13*, 20653–20661.
- (14) Wang, Z.; Cong, Y.; Fu, J. Stretchable and Tough Conductive Hydrogels for Flexible Pressure and Strain Sensors. *J. Mater. Chem. B* **2020**, *8*, 3437–3459.
- (15) Shi, L.; Jia, K.; Gao, Y.; Yang, H.; Ma, Y.; Lu, S.; Gao, G.; Bu, H.; Lu, T.; Ding, S. Highly Stretchable and Transparent Ionic Conductor with Novel Hydrophobicity and Extreme-Temperature Tolerance. *Research* **2020**, *2020*, 2505619.
- (16) Weng, D.; Xu, F.; Li, X.; Li, S.; Li, Y.; Sun, J. Polymeric Complex-Based Transparent and Healable Ionogels with High Mechanical Strength and Ionic Conductivity as Reliable Strain Sensors. *ACS Appl. Mater. Interfaces* **2020**, *12*, 57477–57485.
- (17) Lai, C.-W.; Yu, S.-S. 3D Printable Strain Sensors from Deep Eutectic Solvents and Cellulose Nanocrystals. *ACS Appl. Mater. Interfaces* **2020**, *12*, 34235–34244.
- (18) Chen, L.; Guo, M. Highly Transparent, Stretchable, and Conductive Supramolecular Ionogels Integrated with Three-Dimensional Printable, Adhesive, Healable, and Recyclable Character. *ACS Appl. Mater. Interfaces* **2021**, *13*, 25365–25373.
- (19) Zhang, S.; Sun, N.; He, X.; Lu, X.; Zhang, X. Physical Properties of Ionic Liquids: Database and Evaluation. *J. Phys. Chem. Ref. Data* **2006**, *35*, 1475–1517.
- (20) Zhang, L. M.; He, Y.; Cheng, S.; Sheng, H.; Dai, K.; Zheng, W. J.; Wang, M. X.; Chen, Z. S.; Chen, Y. M.; Suo, Z. Self-Healing, Adhesive, and Highly Stretchable Ionogel as a Strain Sensor for Extremely Large Deformation. *Small* **2019**, *15*, 1804651.
- (21) Cao, Y.; Morrissey, T. G.; Acome, E.; Allec, S. I.; Wong, B. M.; Keplinger, C.; Wang, C. A Transparent, Self-Healing, Highly Stretchable Ionic Conductor. *Adv. Mater.* **2017**, *29*, 1605099.
- (22) Sun, J.; Lu, G.; Zhou, J.; Yuan, Y.; Zhu, X.; Nie, J. Robust Physically Linked Double-Network Ionogel as a Flexible Bimodal Sensor. *ACS Appl. Mater. Interfaces* **2020**, *12*, 14272–14279.
- (23) Liang, L.; Lv, H.; Shi, X.-L.; Liu, Z.; Chen, G.; Chen, Z.-G.; Sun, G. A Flexible Quasi-Solid-State Thermoelectrochemical Cell with High Stretchability as an Energy-Autonomous Strain Sensor. *Mater. Horiz.* **2021**, *8*, 2750–2760, DOI: 10.1039/d1mh00775k.
- (24) Lee, H. Y.; Cai, Y.; Velioglu, S.; Mu, C.; Chang, C. J.; Chen, Y. L.; Song, Y.; Chew, J. W.; Hu, X. M. Thermochromic Ionogel: A New Class of Stimuli Responsive Materials with Super Cyclic Stability for Solar Modulation. *Chem. Mater.* **2017**, *29*, 6947–6955.
- (25) Liu, X.; Wang, B.; Jin, Z.; Wang, H.; Wang, Q. Elastic Ionogels with Freeze-Aligned Pores Exhibit Enhanced Electrochemical Performances as Anisotropic Electrolytes of All-Solid-State Supercapacitors. *J. Mater. Chem. A* **2015**, *3*, 15408–15412.
- (26) Hyun, W. J.; Thomas, C. M.; Hersam, M. C. Nanocomposite Ionogel Electrolytes for Solid-State Rechargeable Batteries. *Adv. Energy Mater.* **2020**, *10*, 2002135.
- (27) Liang, L.; Chen, X.; Yuan, W.; Chen, H.; Liao, H.; Zhang, Y. Highly Conductive, Flexible, and Nonflammable Double-Network Poly(Ionic Liquid)-Based Ionogel Electrolyte for Flexible Lithium-Ion Batteries. *ACS Appl. Mater. Interfaces* **2021**, *13*, 25410–25420.
- (28) Liu, K.; Zhang, Y.; Cao, H.; Liu, H.; Geng, Y.; Yuan, W.; Zhou, J.; Wu, Z. L.; Shan, G.; Bao, Y.; Zhao, Q.; Xie, T.; Pan, P. Programmable Reversible Shape Transformation of Hydrogels Based on Transient Structural Anisotropy. *Adv. Mater.* **2020**, *32*, 2001693.
- (29) Gong, H.; Zhao, Y.; Shen, X.; Lin, J.; Chen, M. Organocatalyzed Photocontrolled Radical Polymerization of Semifluorinated (Meth)Acrylates Driven by Visible Light. *Angew. Chem., Int. Ed.* **2018**, *57*, 333–337.
- (30) Koiry, B. P.; Klok, H.-A.; Singha, N. K. Copolymerization of 2,2,3,3,4,4,4-Heptafluorobutyl Acrylate with Butyl Acrylate ViaRAFT Polymerization. *J. Fluorine Chem.* **2014**, *165*, 109–115.
- (31) Lan, J.; Li, Y.; Yan, B.; Yin, C.; Ran, R.; Shi, L.-Y. Transparent Stretchable Dual-Network Ionogel with Temperature Tolerance for High-Performance Flexible Strain Sensors. *ACS Appl. Mater. Interfaces* **2020**, *12*, 37597–37606.
- (32) Sahrash, R.; Siddiq, A.; Razaq, H.; Iqbal, T.; Qaisar, S. PVDF Based Ionogels: Applications Towards Electrochemical Devices and Membrane Separation Processes. *Heliyon* **2018**, *4*, No. e00847.

- (33) Guyot, B.; Ameduri, B.; Boutevin, B.; Melas, M.; Viguier, M.; Collet, A. Kinetics of Homopolymerization of Fluorinated Acrylates, 5. Influence of the Spacer between the Fluorinated Chain and the Ester Group. *Macromol. Chem. Phys.* **1998**, *199*, 1879–1885.
- (34) Yu, Z.; Wu, P. Underwater Communication and Optical Camouflage Ionogels. *Adv. Mater.* **2021**, *33*, 2008479.
- (35) Zheng, Y.; Chen, S.; Zhang, K. A. I.; Zhu, J.; Xu, J.; Zhang, C.; Liu, T. Ultrasound-Triggered Assembly of Covalent Triazine Framework for Synthesizing Heteroatom-Doped Carbon Nanoflowers Boosting Metal-Free Bifunctional Electrocatalysis. *ACS Appl. Mater. Interfaces* **2021**, *13*, 13328–13337.
- (36) Liu, Z.; Wang, X.; Wei, S.; Lv, H.; Zhou, J.; Peng, P.; Wang, H.; Chen, G. A Wavy-Structured Highly Stretchable Thermoelectric Generator with Stable Energy Output and Self-Rescuing Capability. *CCS Chem.* **2021**, *3*, 2404–2414.
- (37) Forster-Tonigold, K.; Kim, J.; Bansmann, J.; Groß, A.; Buchner, F. Model Studies on the Formation of the Solid Electrolyte Interphase: Reaction of Li with Ultrathin Adsorbed Ionic-Liquid Films and Co<sub>3</sub>O<sub>4</sub>(111) Thin Films. *ChemPhysChem* **2021**, *22*, 441–454.
- (38) Iborra, A.; Díaz, G.; López, D.; Giussi, J. M.; Azzaroni, O. Copolymer Based on Lauryl Methacrylate and Poly(Ethylene Glycol) Methyl Ether Methacrylate as Amphiphilic Macrosurfactant: Synthesis, Characterization and Their Application as Dispersing Agent for Carbon Nanotubes. *Eur. Polym. J.* **2017**, *87*, 308–317.
- (39) Hao, G.; Zhu, L.; Yang, W.; Chen, Y. Investigation on the Film Surface and Bulk Properties of Fluorine and Silicon Contained Polyacrylate. *Prog. Org. Coat.* **2015**, *85*, 8–14.
- (40) Zhang, Y.; Li, M.; Qin, B.; Chen, L.; Liu, Y.; Zhang, X.; Wang, C. Highly Transparent, Underwater Self-Healing, and Ionic Conductive Elastomer Based on Multivalent Ion–Dipole Interactions. *Chem. Mater.* **2020**, *32*, 6310–6317.
- (41) Niu, W.; Zhu, Y.; Wang, R.; Lu, Z.; Liu, X.; Sun, J. Remalleable, Healable, and Highly Sustainable Supramolecular Polymeric Materials Combining Superhigh Strength and Ultrahigh Toughness. *ACS Appl. Mater. Interfaces* **2020**, *12*, 30805–30814.
- (42) Yiming, B.; Guo, X.; Ali, N.; Zhang, N.; Zhang, X.; Han, Z.; Lu, Y.; Wu, Z.; Fan, X.; Jia, Z.; Qu, S. Ambiently and Mechanically Stable Ionogels for Soft Ionotronics. *Adv. Funct. Mater.* **2021**, *31*, 2102773.
- (43) Wang, A.; Wang, Y.; Zhang, B.; Wan, K.; Zhu, J.; Xu, J.; Zhang, C.; Liu, T. Hydrogen-Bonded Network Enables Semi-Interpenetrating Ionic Conductive Hydrogels with High Stretchability and Excellent Fatigue Resistance for Capacitive/Resistive Bimodal Sensors. *Chem. Eng. J.* **2021**, *411*, 128506.
- (44) Shi, L.; Zhu, T.; Gao, G.; Zhang, X.; Wei, W.; Liu, W.; Ding, S. Highly Stretchable and Transparent Ionic Conducting Elastomers. *Nat. Commun.* **2018**, *9*, 2630.
- (45) Wang, Y.; Liu, Y.; Plamthottam, R.; Tebyetekerwa, M.; Xu, J.; Zhu, J.; Zhang, C.; Liu, T. Highly Stretchable and Reconfigurable Ionogels with Unprecedented Thermoplasticity and Ultrafast Self-Healability Enabled by Gradient-Responsive Networks. *Macromolecules* **2021**, *54*, 3832–3844.
- (46) Qu, X.; Niu, W.; Wang, R.; Li, Z.; Guo, Y.; Liu, X.; Sun, J. Solid-State and Liquid-Free Elastomeric Ionic Conductors with Autonomous Self-Healing Ability. *Mater. Horiz.* **2020**, *7*, 2994–3004.
- (47) Sun, T. L.; Kurokawa, T.; Kuroda, S.; Ihsan, A. B.; Akasaki, T.; Sato, K.; Haque, M. A.; Nakajima, T.; Gong, J. P. Physical Hydrogels Composed of Polyampholytes Demonstrate High Toughness and Viscoelasticity. *Nat. Mater.* **2013**, *12*, 932–937.
- (48) Zhou, X.; Guo, B.; Zhang, L.; Hu, G.-H. Progress in Bio-Inspired Sacrificial Bonds in Artificial Polymeric Materials. *Chem. Soc. Rev.* **2017**, *46*, 6301–6329.
- (49) Luo, F.; Sun, T. L.; Nakajima, T.; Kurokawa, T.; Zhao, Y.; Sato, K.; Ihsan, A. B.; Li, X.; Guo, H.; Gong, J. P. Oppositely Charged Polyelectrolytes Form Tough, Self-Healing, and Rebuildable Hydrogels. *Adv. Mater.* **2015**, *27*, 2722–2727.
- (50) Peng, Y.; Zhao, L.; Yang, C.; Yang, Y.; Song, C.; Wu, Q.; Huang, G.; Wu, J. Super Tough and Strong Self-Healing Elastomers Based on Polyampholytes. *J. Mater. Chem. A* **2018**, *6*, 19066–19074.
- (51) Yang, Y.; Wang, X.; Yang, F.; Wang, L.; Wu, D. Highly Elastic and Ultratough Hybrid Ionic-Covalent Hydrogels with Tunable Structures and Mechanics. *Adv. Mater.* **2018**, *30*, 1707071.
- (52) Mackanic, D. G.; Yan, X.; Zhang, Q.; Matsuhisa, N.; Yu, Z.; Jiang, Y.; Manika, T.; Lopez, J.; Yan, H.; Liu, K.; Chen, X.; Cui, Y.; Bao, S. Decoupling of Mechanical Properties and Ionic Conductivity in Supramolecular Lithium Ion Conductors. *Nat. Commun.* **2019**, *10*, 5384.
- (53) Song, H.; Sun, Y.; Zhu, J.; Xu, J.; Zhang, C.; Liu, T. Hydrogen-Bonded Network Enables Polyelectrolyte Complex Hydrogels with High Stretchability, Excellent Fatigue Resistance and Self-Healability for Human Motion Detection. *Composites, Part B* **2021**, *217*, 108901.
- (54) Tang, P.; Yan, H.; Chen, L.; Wu, Q.; Zhao, T.; Li, S.; Gao, H.; Liu, M. Anisotropic Nanocomposite Hydrogels with Enhanced Actuating Performance through Aligned Polymer Networks. *Sci. China Mater.* **2020**, *63*, 832–841.
- (55) Liu, D.; Dong, X.; Han, B.; Huang, H.; Qi, M. Cellulose Nanocrystal/Collagen Hydrogels Reinforced by Anisotropic Structure: Shear Viscoelasticity and Related Strengthening Mechanism. *Compos. Commun.* **2020**, *21*, 100374.
- (56) Li, L.; Zhang, Y.; Lu, H.; Wang, Y.; Xu, J.; Zhu, J.; Zhang, C.; Liu, T. Cryopolymerization Enables Anisotropic Polyaniline Hybrid Hydrogels with Superelasticity and Highly Deformation-Tolerant Electrochemical Energy Storage. *Nat. Commun.* **2020**, *11*, 62.
- (57) Zhang, B.; Zhang, X.; Wan, K.; Zhu, J.; Xu, J.; Zhang, C.; Liu, T. Dense Hydrogen-Bonding Network Boosts Ionic Conductive Hydrogels with Extremely High Toughness, Rapid Self-Recovery, and Autonomous Adhesion for Human-Motion Detection. *Research* **2021**, *2021*, 9761625.
- (58) Mao, J.; Zhao, C.; Li, Y.; Xiang, D.; Wang, Z. Highly Stretchable, Self-Healing, and Strain-Sensitive Based on Double-Crosslinked Nanocomposite Hydrogel. *Compos. Commun.* **2020**, *17*, 22–27.
- (59) Herath, M. B.; Hickman, T.; Creager, S. E.; DesMarteau, D. D. A New Fluorinated Anion for Room-Temperature Ionic Liquids. *J. Fluorine Chem.* **2011**, *132*, 52–56.
- (60) Liu, C.; Li, J.; Jin, Z.; Hou, P.; Zhao, H.; Wang, L. Synthesis of Graphene-Epoxy Nanocomposites with the Capability to Self-Heal Underwater for Materials Protection. *Compos. Commun.* **2019**, *15*, 155–161.
- (61) Cao, Z.; Liu, H.; Jiang, L. Transparent, Mechanically Robust, and Ultrastable Ionogels Enabled by Hydrogen Bonding between Elastomers and Ionic Liquids. *Mater. Horiz.* **2020**, *7*, 912–918.
- (62) Yiming, B.; Han, Y.; Han, Z.; Zhang, X.; Li, Y.; Lian, W.; Zhang, M.; Yin, J.; Sun, T.; Wu, Z.; Li, T.; Fu, J.; Jia, Z.; Qu, S. A Mechanically Robust and Versatile Liquid-Free Ionic Conductive Elastomer. *Adv. Mater.* **2021**, *33*, 2006111.
- (63) Li, R. a.; Fan, T.; Chen, G.; Zhang, K.; Su, B.; Tian, J.; He, M. Autonomous Self-Healing, Antifreezing, and Transparent Conductive Elastomers. *Chem. Mater.* **2020**, *32*, 874–881.
- (64) Ming, X.; Shi, L.; Zhu, H.; Zhang, Q. Stretchable, Phase-Transformable Ionogels with Reversible Ionic Conductor–Insulator Transition. *Adv. Funct. Mater.* **2020**, *30*, 2005079.
- (65) Wang, Y.; Tebyetekerwa, M.; Liu, Y.; Wang, M.; Zhu, J.; Xu, J.; Zhang, C.; Liu, T. Extremely Stretchable and Healable Ionic Conductive Hydrogels Fabricated by Surface Competitive Coordination for Human-Motion Detection. *Chem. Eng. J.* **2021**, *420*, 127637.